ACS APPLIED MATERIALS & INTERFACES

www.acsami.org Research Article

Low-Load Metal-Assisted Catalytic Etching Produces Scalable Porosity in Si Powders

Konstantin Tamarov, Riku Kiviluoto, Joseph D. Swanson, Bret A. Unger, Alexis T. Ernst, Mark Aindow, Joakim Riikonen, Vesa-Pekka Lehto, and Kurt W. Kolasinski*

Cite This: *ACS Appl. Mater. Interfaces* 2020, 12, 48969−48981 Read Online

ACCESS | Metrics & More | Article Recommendations | Supporting Information

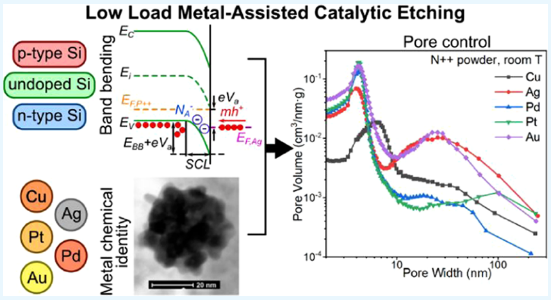

ABSTRACT: The recently discovered low-load metal-assisted catalytic etching (LL-MACE) creates nanostructured Si with controllable and variable characteristics that distinguish this technique from the conventional high-load variant. LL-MACE employs 150 times less metal catalyst and produces porous Si instead of Si nanowires. In this work, we demonstrate that some of the features of LL-MACE cannot be explained by the present understanding of MACE. With mechanistic insight derived from extensive experimentation, it is demonstrated that (1) the method allows the use of not only Ag, Pd, Pt, and Au as metal catalysts but also Cu and (2) judicious combinations of process parameters such as the type of metal, Si doping levels, and etching temperatures facilitate control over yield (0.065−88%), pore size (3−100 nm), specific surface area (20−310 $m^2 \cdot g^{-1}$), and specific pore volume (0.05−1.05 $cm^3 \cdot g^{-1}$). The porous structure of the product depends on the space-charge layer, which is controlled by the Si doping and the chemical identity of the deposited metal. The porous structure was also dependent on the dynamic structure of the deposited metal. A distinctive comet-like structure of metal nanoparticles was observed after etching with Cu, Ag, Pd, and, in some cases, Pt; this structure consisted of 10−50 nm main particles surrounded by smaller (<5 nm) nanoparticles. With good scalability and precise control of structural properties, LL-MACE facilitates Si applications in photovoltaics, energy storage, biomedicine, and water purification.

KEYWORDS: *low-load metal-assisted catalytic etching (MACE), porous silicon, powder, porosity, nanoparticles, silicon nanostructures*

■ INTRODUCTION

Metal-assisted catalytic etching (also known as metal-assisted etching or metal-assisted chemical etching), MACE, is a simple and versatile method of Si micropatterning. Nanostructuring of Si with MACE has attracted considerable attention in the past few years to fabricate nonreflecting surfaces for photovoltaics,[1−3] to prepare patterned structures for sensing,[4−6] and to overcome the huge volume expansion of Si-based Li-ion battery anodes.[7−9] Porous Si nanowires (NWs) and nanoneedles formed by MACE have been used in a large number of different biological applications including sensing,[10] studies of cell−Si interfaces,[11,12] and therapeutic delivery.[13−15]

Typically, MACE is performed in a two-step process (metal deposition and etching are performed separately)[16] although one-step MACE (combined metal deposition and etching)[17,18] has also been demonstrated successfully. In the two-step process, a piece of Si is first immersed into a metal plating solution consisting of hydrofluoric acid (HF), water, and dissolved metal salt, e.g., $AgNO_3$. Ag^+ ions deposit as particles, dendrites, or layers on the Si surface, and this process can be further controlled by applying masks or even more sophisticated methods such as lithography, thermal decomposition, or sputtering. In the second step, the Si is immersed in a solution containing HF and oxidant, usually H_2O_2. The metal catalyst facilitates hole injection into the Si valence band, which controls the rate of the etching reaction as long as the concentration of HF is sufficiently high.

Due to the high concentrations of holes near the metal/Si interface and generally high metal coverage, the most common outcome of MACE is the formation of 80−150 nm etch track pores bored by the cooperative motion of metal particles, which are formed dynamically at the beginning of etching.[19,20] The walls of the pores are often called Si NWs, even though etching first forms interconnected walls and ridge-like structures that are cleaved readily by, e.g., ultrasound or capillary forces to form stand-alone Si NWs.

In an attempt to improve the cost-efficiency of the MACE process, several recent studies focused on etching inexpensive Si grains, chunks, and powders instead of wafers. It is especially interesting that even in powders, metal particles still move cooperatively, descend into Si perpendicular to particular

Received: August 3, 2020
Accepted: October 2, 2020
Published: October 14, 2020

facets,[19] and produce etch track pores and Si NWs similar to MACE of wafers.

Thus, MACE was applied to inexpensive and relatively impure metallurgical-grade (MG) powders. Preferential etching of the impurities led to purification of Si,[21,22] which made it possible to apply the etched particles for Li-ion battery anodes[23,24] and photovoltaics[25] and to produce biocompatible nanostructures for nanomedicine.[26]

Scaling up MACE of powders requires control of the etching process. The rate of this highly exothermic reaction is proportional to the surface area. The high surface area of powders compared to that of Si wafers leads to considerable heat production during MACE. Thermal management during the reaction is crucial to improve the uniformity and reproducibility of the product. Similar to regenerative electroless etching (ReEtching),[27] we exploited a syringe pump to inject oxidant at a constant rate, giving better control over MACE and avoiding excessive heating. In addition, we demonstrated the use of a syringe pump to deposit Ag controllably. Combined with vigorous stirring of Si powder and addition of acetic acid to HF, we achieved uniform Ag deposition over a wide range of $n(\mathrm{Ag})\cdot A_{\mathrm{Si}}{}^{-1}$, from 10 to 0.002 $\mathrm{mmol\cdot m^{-2}}$, where $n(\mathrm{Ag})$ is the amount of silver and A_{Si} is the surface area of the Si powder subjected to MACE.[20]

Varying the Ag coverage, we demonstrated that large etch track pores produced by the correlated motion of metal catalyst nanoparticles and Si NWs are not the only outcome of Ag MACE.[20] When the Ag amount is low in the depositing solution ($n(\mathrm{Ag})\cdot A_{\mathrm{Si}}{}^{-1} \leq 0.06$ $\mathrm{mmol\cdot m^{-2}}$), Ag deposits as individual 10−20 nm nanoparticles instead of a thick layer of interconnected clusters and dendrites. During etching, these small nanoparticles move in an uncorrelated manner producing random pores with 10−20 nm diameter and, if the p-type doping level is high enough, 4−6 nm tortuous pores. Thus, a mesoporous layer is formed in contrast to Si NWs. We call this regime low-load MACE or LL-MACE to emphasize its difference from conventional high-load MACE or HL-MACE.

For a comprehensive discussion of HL-MACE, and structures accessible through this process, we refer to the recent review by Alhmoud et al.[28] Here, we summarize a few salient points. Depending on the metal catalyst, Si doping level, and oxidant amount, the porosity of etch track pore walls and Si NWs in HL-MACE can be varied. Etching highly doped p-type Si ($\rho = 0.01$−0.02 $\Omega\cdot\mathrm{cm}$) with Ag generally resulted in NWs with porous walls, while lower doping levels led to solid Si NWs.[29,30] Etching with Au produced porous Si NWs for a Si resistivity of up to 1 $\Omega\cdot\mathrm{cm}$, depending on the H_2O_2 concentration.[31] Pt formed both a porous layer and helical etch track pores on 10 $\Omega\cdot\mathrm{cm}$ p-type wafers; the latter was attributed to the multifaceted crystalline shape of the Pt particles. Pd was found to be more convoluted than others as it catalyzed etching even without an oxidant and resulted in electropolishing of Si.[32−34] HL-MACE with Cu never produced defined etch track pores[35,36] and Si NWs, except in the case of electrochemical etching under applied bias.[37] This is due to the low electronegativity and reduction potential of Cu compared to those of other metals, which prevents efficient deposition and leads to enhanced dissolution during etching. Overall, depending on the chemical identity of the metals, their catalytic activity toward the reduction of H_2O_2, and induced band bending,[33,38,39] different morphologies were produced by HL-MACE.

Herein, we present a comprehensive study of LL-MACE of Si powders, where we use low amounts of Cu, Ag, Au, Pt (12 $\mu\mathrm{mol\cdot m^{-2}}$), and Pd (1.2 $\mu\mathrm{mol\cdot m^{-2}}$) to etch mesopores. Various Si grades were used including powders prepared from P++, P+, P, N+, N++, and undoped wafers (UW) as well as metallurgical-grade powders with either 99.6% (MG) or 99.997% (MC10) purity. We demonstrate that by choosing Si grade, metal, and temperature, one can vary over a wide range the yield (0.065−88%), pore size (3−100 nm), surface area (20−310 $\mathrm{m^2\cdot g^{-1}}$), and pore volume (0.05−1.05 $\mathrm{cm^3\cdot g^{-1}}$).

Overall, we found a great variety of porosity after LL-MACE. This can be applied to optimize porosity and surface area for applications such as Si-based Li-ion battery anodes, antireflection coatings for photovoltaics, and to load drugs or biomolecules of a specific size. Furthermore, LL-MACE is easy to scale up, uses minimal amounts of metal, and works well for certain Si grades with Cu, opening a pathway to significantly less expensive processing.

■ EXPERIMENTAL SECTION

Samples were prepared and characterized in line with previously published methods.[20,32,40] Briefly, Si powders of known purity/doping levels were milled and cleaned prior to the deposition and nucleation of a metal catalyst. Subsequently, etching was initiated by the addition of oxidant (H_2O_2). Both nucleation and etching were aided by the use of acetic acid as a surfactant and steady metered injection of dissolved metal ions or H_2O_2 with a syringe pump. The sample temperature during reaction was regulated by immersing the reaction vessel in either an ice/water or temperature-controlled water bath. After well-defined rinsing and drying procedures, the samples were characterized by plain-view and cross-sectional scanning electron microscopy (SEM) with focused ion beam (FIB) cutting. FIB sectioning was also used to prepare samples for transmission electron microscopy (TEM). Further characterization was performed with N_2 sorption followed by analysis with the Brunauer−Emmett−Teller (BET) model and Barrett−Joyner−Halenda (BJH) theory. The detailed methods can be found in the Supporting Information.

■ RESULTS

Controlled injection together with acetic acid as a surfactant resulted in the uniform coverage of Si surfaces with individual 5−30 nm metal nanoparticles separated by similarly sized gaps.[20,32] Specifically for Ag,[20] we found deposited nanoparticles with a mean size of 19.0 ± 9.5 nm and a center-to-center separation of 25.6 ± 9.0 nm (uncertainty given as 1 standard deviation) to be responsible for catalyzing efficient etching in the LL-MACE regime. These values were calculated under the assumption that the particle surfaces were perfectly planar. As shown previously,[20] these well-spaced nanoparticles move in a completely uncorrelated manner during etching, following paths determined by the minimum energy required to etch out one atomic plane of Si.[19]

In the etching step of LL-MACE, the H_2O_2 solution was also injected in a controlled manner using a syringe pump; this provided a minimal steady-state supply of the oxidant that significantly reduced the rate of heat generation. In most cases, the temperature of the etching solution did not exceed the temperature of cooling the bath by more than 12 °C. It should be stressed that, while Ag, Pd, Pt, and Au are commonly applied in HL-MACE,[16] Cu is never used because it fails to deposit on Si in a sufficient quantity and it dissolves efficiently in the presence of excess H_2O_2. However, the use of a syringe pump for the dosing of H_2O_2 enables us to reduce its steady-state concentration to a level that does not remove Cu nanoparticles from the etch front.

Application of different metals in LL-MACE resulted in distinctive morphologies of etched pores, yet they also had some common features. Top-view SEM images (Figure 1 and Sections S3−S6, Supporting Information) show that Cu and Pt keep the Si particle surfaces flat and edges sharp. A unique feature of Pt particles is that they tend to move laterally across the Si surface producing many, sometimes helical channels before descending into Si. Ag, Pd, and Au, on the other hand, smoothen Si edges while roughening initially flat facets, which produces a fuzzy appearance that is distinctly different from the texture of particles produced by HL-MACE.

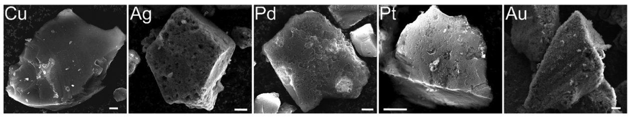

Figure 1. General view of 11−25 μm MG Si particles after LL-MACE with Cu, Ag, Pd, Pt, and Au. The scale bar represents 2 μm.

Cross-sectional images are presented in Figure 2. An enlarged version of Figure 2 with additional annotation can be found in the Supporting Information (Figure S2.1). These images reveal that the etched Si for all metals consisted of two distinct regions: (1) etch track pores in the direction of the metal nanoparticle movement and (2) a layer of tortuous pores surrounding the tracks or extending deep into Si. The tortuous pores were similar to those observed in ReEtching of Si powders, where no metal catalyst was deposited on P++ and MG Si.[27] For Cu, Ag, and Pd, tortuous pore regions tended to surround etch track pores making the boundary between etched and bulk Si uneven, composed of connected spherical regions. Cu nanoparticles sometimes were not surrounded by tortuous pores. In contrast, the boundary between tortuous pores and bulk Si for Pt and Au was remarkably flat despite different Pt and Au particle morphologies (Figure 2). The observation of both etch track and tortuous pores is consistent with previous results such as those of Hochbaum et al.,[41] who were the first to observe porous nanowire formation, Chiappini et al.,[31] and Patil et al.[42]

The dynamic nature of the metal nanoparticle structure caused by the etch process is illustrated by a comet-like structure reported here for the first time (Figures 2 and S2.1 and Sections S3−S6, Supporting Information). Cu and Pd nanoparticles had rather smooth although not round surfaces, and they were always followed by a halo of small <5 nm nanoparticles. The large metal nanoparticles form the cores of these comet-like structures; they were 50−80 nm for Cu and 30−50 nm for Pd. Interestingly, Cu "comets" have small nanoparticle "tails" behind their etch track, while Pd "comet" cores were surrounded by small nanoparticles on all sides. Pt particles possessed rich irregular structures, which appear to form by aggregation at the beginning of etching when particles moved extensively along the Si surfaces. These aggregates expose different Pt crystalline planes, which, we suggest, make the change of etch direction easy and, in some cases, produce helical cavities. Despite the previously considered stability of Pt particles during MACE, they sometimes, although not always, showed comet-like structures and were surrounded by small nanoparticle satellites. Au nanoparticles were the most stable and round; they never showed a halo of small nanoparticles and kept their sizes in the range of 10−40 nm during etching.

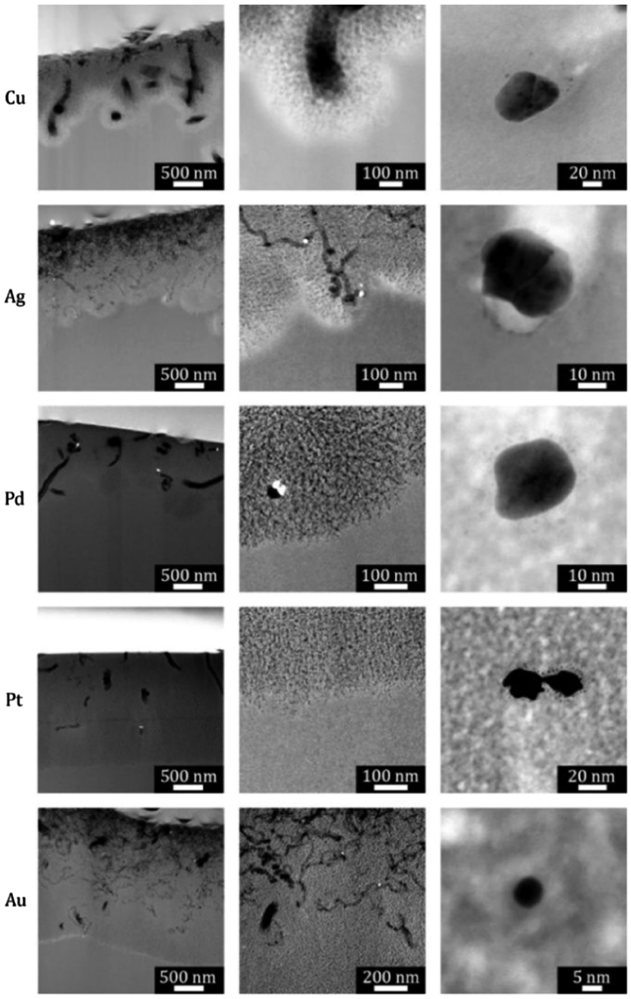

Figure 2. Cross-sectional bright-field (BF) and high-angle annular dark-field (HAADF) scanning transmission electron microscopy (STEM) images after LL-MACE of 11−25 μm P++ (for Cu) and 2−44 μm MG (for other metals) powders in an ice bath. The left column (HAADF, metal appears light) shows the border between the bulk and etched Si: Cu and Pd produce an irregular border and tortuous pores surrounding metal particles; Pt and Au present a sharp and uniform border between the porous layer and solid core. The middle column (HAADF) takes a closer look at the porous layer showing both etch track pores produced by the metal particle movement and tortuous mesopores produced by remote etching. The right column (BF, metal appears dark) depicts the structure of metal particles: Cu and Pd always present a halo of small particles following big ones; Pt sometimes presents a halo of small particles and the large particles have an irregular structure; Au never shows the halo. An enlarged, annotated version of this figure and more images of metal particles are shown in the Supporting Information.

The outcomes of LL-MACE changed dramatically with the metal catalyst, Si grade (Table 1), and temperature (Figure 3 and Sections S3−S12, Supporting Information). In SEM images, Cu displays the most prominent change in structure with the increasing temperature. For low-temperature (LT) etching in an ice bath, Cu particles descend into Si and produce pores. At high temperature (HT, water bath at 43 °C), most of the Si becomes electropolished: P++, MG, and MC10 present broken Si pieces with smooth surfaces, while UW and N++ have macropores with crystallographically defined edges. N++ powder additionally presents numerous uniformly distributed openings of tortuous pores at HT (Figures 3 and S3.10, Supporting Information). Other metals demonstrate less pronounced differences between LT and HT. One can notice similarity for powders etched with Ag and Au. Pd and Pt show distinctive morphologies, which, however, look similar for all Si grades. Pt is the only case that

Table 1. Summary of the Si Particle Sizes and Grades Used in LL-MACE[a]

abbreviation	resistivity ($\Omega\cdot$cm)	doping type	doping density (cm^{-3})	particle size (μm)
P++[b]	0.0186	boron	4×10^{18}	11–25
P+[b]	0.105	boron	3×10^{17}	11–25
P[b]	25	boron	5×10^{14}	11–25
UW[b]	>5000	boron	$<1 \times 10^{12}$	11–25
N+[b]	1.15	phosphorus	3×10^{15}	11–25
N++[b]	0.0144	phosphorus	3×10^{18}	11–25
MG[c,d]		Fe/Ti/Ca/Al		11–25
MC10[c,e]		Fe/Ti/Ca/Al		1.5–10

[a] Dopant concentrations were calculated using the Caughey–Thomas expression[43] for electron and hole mobilities. [b] Ground single-crystal (100) wafers from Okmetic Oy, Finland. [c] Metallurgical-grade Si from Elkem Silicon Materials, Norway. [d] Purity: 99.8%. [e] Purity: 99.997%.

allows easy observation of the openings of tortuous pores on SEM images and the increase of their diameters with the increase of temperature.

Measured pore size distributions for P++, UW, and N++ powders (Figure 4) and for MG and MC10 powders (Figure S13.1, Supporting Information) after LL-MACE at three temperatures reveal quantitative insights into the structure of etched Si because the presence or absence of tortuous pores (<10 nm) can be easily recognized. It should be noted here that the Barrett–Joyner–Halenda (BJH) analysis applied to N_2 desorption isotherms is not sensitive for large pores (>75 nm). Therefore, etch track pores, for example, produced by Pt particles, are not visible in the pore size distributions.

Cu is the metal with the lowest reduction potential, and it readily dissolves especially at HT, when holes are injected into it at a higher rate than at LT and room temperature (RT). Consequently, it may be anticipated that Cu LL-MACE either (1) partially follows a ReEtching-like mechanism where Cu ions inject holes into Si directly and then get regenerated by H_2O_2 to repeat the process and/or (2) preferentially adsorb at step and defect sites on the Si surfaces akin to underpotential deposition, which in turn causes step-flow etching rather than porosification. The latter observation is consistent with the observation of crystallographically defined etched features noted above. The combination of these effects results in complete electropolishing of Si at HT. At LT, Cu is capable of producing tortuous pores for highly doped P++ and N++ powders (Figure 4) and MG (Section S3, Supporting Information). The increase of the etching temperature to RT and HT for P++ Si results in the formation of mostly etch track pores by comet-like particles. In the case of N++ powder, tortuous pores were observed at all temperatures. Their volume was the highest in N++ among all Si grades and their average width increased with the temperature. We attribute this to the partial recombination of injected holes, which prevented electropolishing. For UW wafer, a minor component of etching is the formation of pores below 100 nm, while macropore formation represents the majority (Figure 3).

Use of Ag significantly changes the outcome of LL-MACE compared to that of Cu-catalyzed etching (Figure 4 and Section S4, Supporting Information). The volume of tortuous pores for P++ powder at LT (0.037 cm$^3\cdot$g^{-1}) is much smaller than for Cu (0.18 cm$^3\cdot$g^{-1}; Tables S3.2 and S4.2, Supporting Information) and increases with increasing temperature (note the different *y*-axis scales in the graphs). Etch track pores produced by 10–30 nm Ag particles are clearly visible. They become wider at HT, possibly due to high hole injection and Si polarization, which results in an additional etching around Ag particles and thus pore widening. In UW powder, Ag is only able to make etch track pores, while in N++ tortuous pores were observed again and in higher volume than in P++.

Pd is the most peculiar among the metals. Pd loading had to be decreased by a factor of 10 to avoid complete Si dissolution. Pd was found to create a moderate number of tortuous pores in P++ and a high number in N++ powder, while UW powder is mostly electropolished (Figure 4). The average pore width increased for the former cases with the increase of temperature along with the decrease of volume. We attribute this to the enhanced electropolishing triggered by a higher rate of hole injection into Si at RT and HT. N++ Si at HT was completely dissolved (yield was 0.06%). Etch track pores were hardly

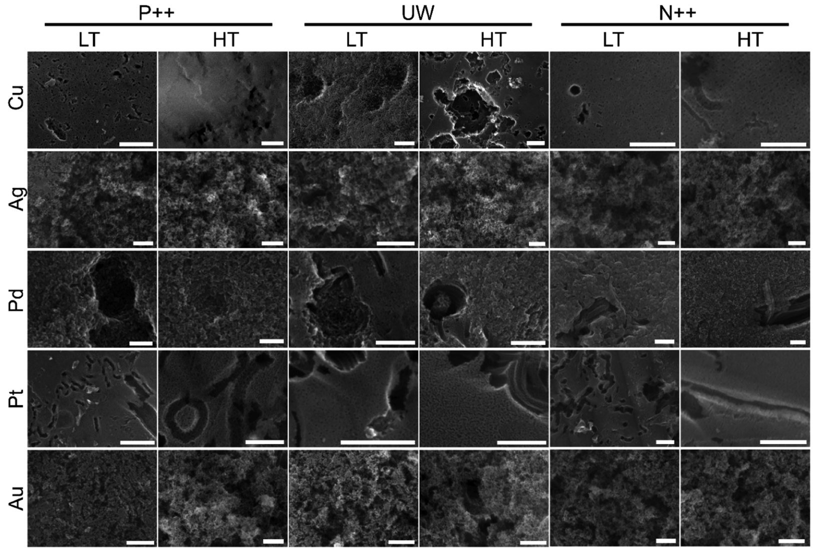

Figure 3. SEM images of the outer surfaces of Si particles after LL-MACE of P++, UW, and N++ 11–25 μm powders with different metals. Low-temperature (LT) and high-temperature (HT) columns show particles etched in an ice bath and water bath at 43 °C, respectively. The scale bar represents 200 nm.

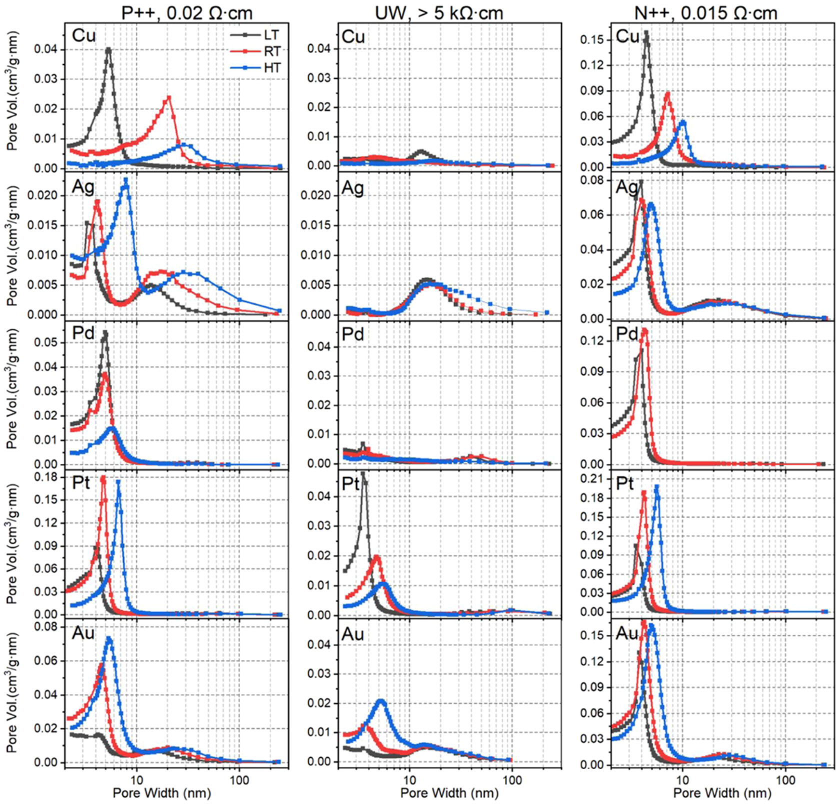

Figure 4. BJH pore size distributions of P++, UW, and N++ powders after Cu, Ag, Pd, Pt, and Au LL-MACE at three different temperatures: low temperature (LT, ice bath), room temperature (RT, water bath), and high temperature (HT, water bath at 43 °C).

observed (small peak around 40−50 nm) in the few Si particles that remain.

Pt and Au are the two metals that could etch tortuous pores in all Si grades (Figure 4). Notably, Pt did not distinguish between P++ and N++ powders. Pore sizes and volumes are very similar in both cases; the average pore widths and volumes increased with the increase of etching temperature. In Au LL-MACE, tortuous pore volumes for N++ powder were 1.6 ± 0.1 times higher than for P++. Pore volumes, just as for Pt, grew with the increase in temperature. However, for UW powder, the pore size and volume change as a function of temperature are opposite for Pt and Au. While for Pt the volume of tortuous pores decreases from 0.17 to 0.04 $cm^3 \cdot g^{-1}$, for Au it grows from 0.02 to 0.11 $cm^3 \cdot g^{-1}$ with the change from LT to HT. Note here again the clear presence of etch track pores produced by 10−40 nm Au nanoparticles similar to that of the Ag ones. This explains the resemblance between SEM images in Figure 2 for Ag and Au. However, that is the only resemblance between them; Au clearly outperforms Ag in the etching of tortuous <10 nm pores for all Si grades.

The specific characteristics of P++, UW, and N++ powders after LL-MACE are summarized in Figure 5, and for MG and MC10 powders in Figure S13.2 (Supporting Information). It can be seen that applying different metals, Si grades, and temperatures, a wide range of specific surface areas, pore volumes, and yields are accessible through LL-MACE. Depending on the etching parameters, surface areas were found to vary from 14 to 310 $m^2 \cdot g^{-1}$, pore volumes from 0.07 to 1.03 $cm^3 \cdot g^{-1}$, and yields from 0.06 to 80%. The lowest values for surface areas and pore volumes were measured for Cu and Pd, especially for UW powder at HT. The highest values were unexpectedly measured for N++ powder etched with Au. Yields were the lowest when electropolishing appeared, particularly for Cu and Pd at HT.

A general correlation between specific surface area and pore volume can be observed; their increase (or decrease) correlates with each other in most etchings. Yield, however, does not show such a good correlation in many cases. This discrepancy is because pore volumes were quantified with N_2 sorption and calculated using the BJH method, which is applicable to mesopore and small macropore range (2−75 nm). On the other hand, yield accounts for all Si removed by the etch track pore formation, etching of tortuous pores, and electropolishing. To quantify the relative contribution of mesopores to the total amount of Si etched, we introduce the ratio of v_{pore}/v_{etched}. It connects two measured values: pore volume δ_{pore} from BJH analysis and yield. The ratio can be calculated using the following equation (see the derivation in Section S1.4, Supporting Information)

$$\frac{v_{pore}}{v_{etched}} = \frac{\delta_{pore}\rho_{Si} Y}{(1 - Y)} \times 100\% \tag{1}$$

where δ_{pore} $[cm^3 \cdot g^{-1}]$ is the specific BJH pore volume, i.e., the volume of pores significantly smaller than ∼100 nm, $\rho_{Si} = 2.33$ $g \cdot cm^{-3}$ is the bulk density of Si, and Y is the yield.

When v_{pore}/v_{etched} is close to 0%, but the yield is high, most of the etching produced macropores. If v_{pore}/v_{etched} is close to 0% and the yield is also small (Cu and Pd at HT), electropolishing took place. Ag produced only etch track pores in UW powder and v_{pore}/v_{etched} = 10%. High values of v_{pore}/v_{etched} (as high as 50−90%), specific surface area, and pore volume were found for Pt. Thus, Pt is the optimal catalyst to form mostly tortuous <10 nm pores; the large etch track pores visible on SEM images

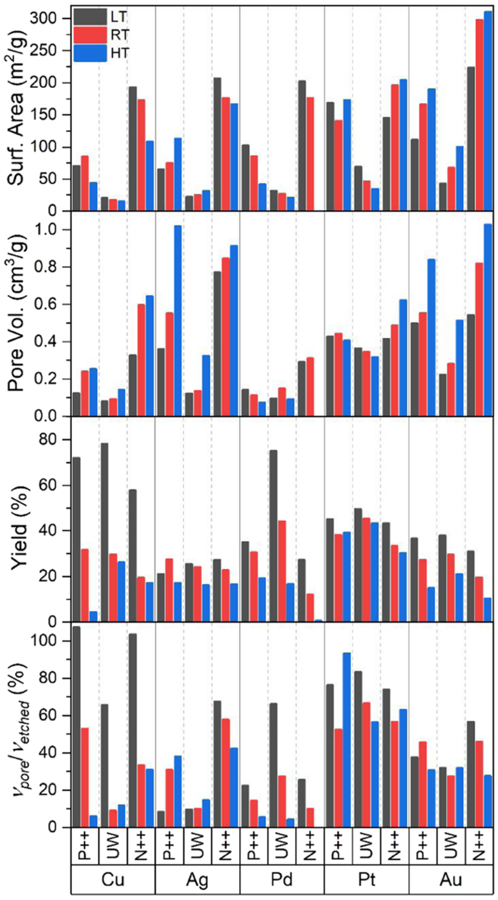

Figure 5. BET specific surface area, yield, BJH pore volume, and ratio of $\nu_{\text{pore}}/\nu_{\text{etched}}$ for P++, UW, and N++ powders after Cu, Ag, Pd, Pt, and Au LL-MACE at three different temperatures. The value of $\nu_{\text{pore}}/\nu_{\text{etched}}$ describes the ratio of the BJH pore volume (pores < 150 nm) to the total volume of etched-out Si.

account for a minority of the etched Si. Pt is, however, limited to producing a relatively small surface area for UW powder.

Au is the optimal catalyst for etching of tortuous pores in all Si grades. It is the metal that created the highest specific surface areas of 310 $m^2 \cdot g^{-1}$ for N++ powder and 190 $m^2 \cdot g^{-1}$ for P++ powder, and it is the only catalyst to produce up to 100 $m^2 \cdot g^{-1}$ surface area and 0.5 $cm^3 \cdot g^{-1}$ pore volume in UW Si at HT. The ratio of $\nu_{\text{pore}}/\nu_{\text{etched}}$ adopts moderate values of 25−50% depending on temperature, possibly due to etch track pores that are larger than 100 nm and/or partial electropolishing.

Finally, we compared all of the Si grades at specific temperatures for all metals to (1) understand the role of impurities in MG and MC10 powders and (2) evaluate the effect of intermediate dopant levels in P+, P, and N+ powders on pore size distributions (Figure 6). The temperatures were selected to avoid electropolishing and to produce a high number of tortuous pores. Specific surface areas, pore volumes, yields, and $\nu_{\text{pore}}/\nu_{\text{etched}}$ values can be found in Section S14, Supporting Information. Figure 6 demonstrates unambiguously that there is a threshold for the appearance of a high volume of tortuous pores. They are etched efficiently in highly doped nearly metallic P++ and N++ powders, as well as 99.6% pure MG Si, independent of the metal catalyst used. Interestingly, N++ outperforms P++ in all cases, although it was generally considered that in MACE remote etching appears mainly in the highly doped p-type Si.[28] All moderately doped Si powders, UW Si, and 99.997% pure MC10 powder show nearly the same outcome. MC10 has somewhat larger pore volumes and surface areas than P+, P, UW, and N+ powders because of the smaller particle size, 1.5−10 μm compared to 11−25 μm for others. Thus, a higher initial exterior surface area is accessible for etching. The only difference between P+, P, UW, and N+ powders can be observed for Pt-etched P+ Si, which has a larger volume of tortuous pores than the others. MG powder is somewhat in between N++ and P++. With Cu, MG resembles N++, while with Au it resembles P++.

DISCUSSION

Mechanism of LL-MACE. The presence of a hole near the Si surface is the essential requirement to initiate Si etching in HF-based solutions. Holes polarize surface Si−H bonds making them susceptible to fluoride ion attack and eventually resulting

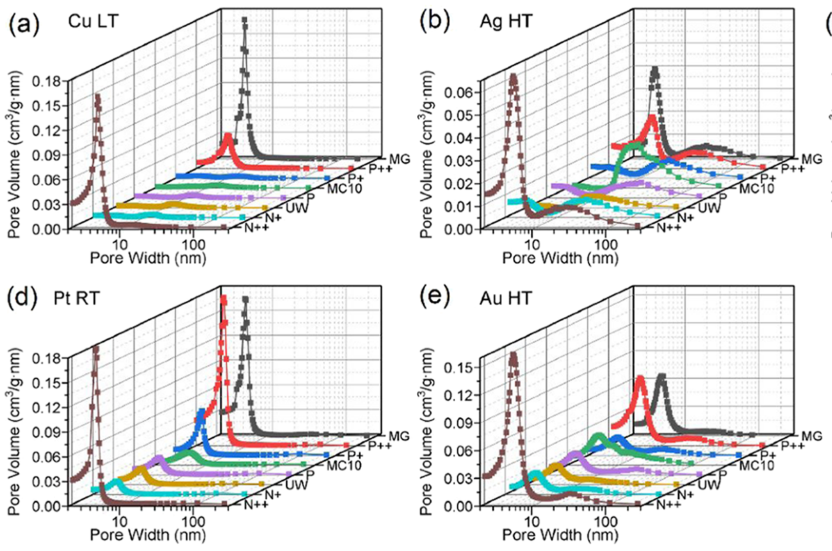

Figure 6. BJH pore size distribution after (a) Cu, (b) Ag, (c) Pd, (d) Pt, and (e) Au LL-MACE of different Si grades at the selected temperatures. The temperatures producing a high volume of tortuous pores are shown.

Table 2. Summary of Band Bending Magnitudes, Types, and Widths of Space-Charge Layers Formed Due to Metal Deposition on Si in an Ideal Case with Doping Types and Densities Used in LL-MACE

Si type \ E_F (eV)[a]	Cu 4.94 eV[b]	Ag 4.74 eV valence 2[c]	Pd 5.6 eV valence 2/4	Pt 5.93 eV valence 4	Au 5.31 eV valence 2
P++	−0.37 eV[d]/8.6 nm[e]	−0.57 eV/10 nm	0.29 eV/1.4 nm	0.62 eV/1.4 nm	0.004 eV/1.4 nm
0.04	P depletion[f]	P depletion	P accumulation/degeneracy	P accumulation/degeneracy	P weak accumulation
P+	−0.3 eV/23 nm	−0.5 eV/28 nm	0.36 eV/5.3 nm	0.69 eV/5.3 nm	0.07 eV/5.3 nm
0.11	P depletion	P depletion	P accumulation/degeneracy	P accumulation/degeneracy	P weak accumulation
P	−0.14/169 nm	−0.34 eV/230 nm	0.52 eV/130 nm	0.85 eV/130 nm	0.23 eV/130 nm
0.27	P depletion	P depletion	P accumulation/degeneracy	P accumulation/degeneracy	P accumulation
UW	0.02/4 μm	−0.18 eV/1.5 μm	0.68 eV/2.9 μm	1.01 eV/2.9 μm	0.39 eV/2.9 μm
0.43	P weak accumulation	P depletion	P accumulation/degeneracy	P accumulation/degeneracy	P accumulation
N+	0.48/320 nm	0.28 eV/250 nm	1.14 eV/200 + 60 nm	1.47 eV/200 + 60 nm	0.85 eV/200 + 60 nm
0.88	N depletion	N depletion	N depletion + inversion	N depletion + inversion	N depletion + inversion
N++	0.66/21 + 6 nm	0.46/9.9 nm	1.32 eV/21 + 6 nm	1.65 eV/21 + 6 nm	1.03 eV/21 + 6 nm
1.06	N depletion + inversion	N depletion	N depletion + inversion	N depletion + inversion	N depletion + inversion

[a] Fermi energy E_F is calculated from the top of the valence band E_V, which is set to 0. Si work function in bulk is $\Phi_{Si} = \chi_{Si} + E_g - E_F$, where χ_{Si} is the Si electron affinity and E_g is the band gap. [b] Metal work functions Φ_M for (111) planes are taken from ref 56. [c] Molar stoichiometry $n(VO_2^+)/n(Si)$ for MACE with VO_2^+.[32] [d] Ideal magnitudes of band bending E_{BB} calculated by subtracting the Si work function Φ_{Si} from metal work function Φ_M. For $E_{BB} < 0$, valence and conduction band edges bend downwards (hole depletion for the p-type Si), for $E_{BB} > 0$—upwards (electron depletion for the n-type Si). [e] Schottky depletion space-charge layer D_{dep} width was calculated using eq S15.1 (Supporting Information). Equation S15.4 was used for inversion layer width. The width of the accumulation layer is the Debye length L_D calculated using eq S15.3. [f] Classification of the space-charge layer based on the doping type, density, and magnitude of band bending E_{BB}.

in the dissolution of Si. Various Si etching methods, including electrochemical anodization, stain etching, and MACE, require holes and they satisfy it using different approaches. In electrochemical anodization of Si, holes present in Si due to doping, light illumination, or spontaneous bulk generation are directed to the surface by an applied bias. To form porous Si, the bias should induce a small enough current density to make the current-doubling pathway of Si dissolution dominant. In this pathway, an injection of 1 hole into the valence band and 1 electron into the conduction band (that is, a valence 2 process) is involved in the dissolution of 1 Si atom.[44] With the increase of bias strength, the current-quadrupling (valence 4) pathway involving 4 holes per Si atom becomes dominant and results in complete dissolution of Si, i.e., above-critical-current density etching. In stain etching, a strong oxidant (such as HNO_3) present in the HF solution is able to oxidize Si directly, thus injecting holes into the valence band.[45] Depending on the concentrations, stain etching can form porous Si or extremely flat surfaces by electropolishing.

In MACE, H_2O_2 is the most commonly used oxidant.[16,28] It has very poor hole injection kinetics into the Si valence band, and the etch rate in HF/H_2O_2 is far below 0.005 nm·s^{-1}[46] for the H_2O_2 concentrations used in this study. The inability of H_2O_2 to induce Si etching directly is possibly due to the need to break H_2O_2 into two −OH radicals for charge transfer to occur. In HF solutions, Si surfaces are H-terminated and cannot dissociate H_2O_2 at an appreciable rate. Thus, a catalyst is necessary to reduce H_2O_2 and to inject holes into Si; many different metals were studied for MACE including most commonly Ag, Au, Pd, Pt,[16,28,32] and Cu[36] and more exotically Ru,[47] Rh,[48] and Ni.[49] Ag and Au are the most frequently applied catalysts, as their high loading forms ordered arrays of Si NWs after HL-MACE. Cu does not deposit well on Si surfaces and dissolves after oxidation with high-concentration H_2O_2, thus making it impossible to etch Si NWs.

The electrochemical reactions involved in MACE consist of a cathodic reaction on the metal catalyst and an anodic reaction on Si. The overall reaction can be written as[16,50]

$$\mathrm{Si} + 6\mathrm{HF} + \frac{n}{2}\mathrm{H_2O_2} \rightarrow \mathrm{H_2SiF_6} + n\mathrm{H_2O} + \frac{4-n}{2}\mathrm{H_2}\uparrow \quad (2)$$

where n can be 2, 3, or 4. $n = 2$ is the valence 2 or current-doubling pathway, which is attributed to the formation of porous Si and porous Si NWs during MACE (or more precisely HL-MACE).[51] When $n = 4$, the current-quadrupling or valence 4 pathway is in action, which can trigger electropolishing[52] or porosification, based on the model first proposed by Kooij and Vanmaekelbergh[53] and explained in detail by Kolasinski et al.[32] $n = 3$ results from a mixture of divalent and tetravalent processes. In HL-MACE, it is believed that etching above the critical current density for porosification occurs in the vicinity of metal particles because the concentration of holes injected into Si is the highest there. However, some of the holes can diffuse further from the metal particles. These holes induce nonlocal or remote etching typically in the current-doubling regime producing porous Si and porous Si NWs.

To determine the prevailing pathway, Chartier et al.[51] suggested using the ratio of HF and H_2O_2 concentrations

$$\rho = \frac{[\mathrm{HF}]}{[\mathrm{HF}] + [\mathrm{H_2O_2}]} \quad (3)$$

They found that for Ag HL-MACE and $\rho \geq 0.8$ the reaction proceeded predominantly according to the valence 2 pathway, while for $\rho \leq 0.2$ a valence 4 pathway and electropolishing were observed with no Si NWs formed. In the middle range of $0.2 \leq \rho \leq 0.8$, the mixture of pathways was present. This is currently the widely accepted view on the HL-MACE mechanism supported by many studies[28,33] and comprehensively investigated for p-type Si wafers.[31]

Applying this criterion to LL-MACE, ρ would be equal to 0.92 if all 0.037 mol of H_2O_2 were added initially to the etching solution. However, ρ is never this large because during injection H_2O_2 reacts at a rate that is comparable to the rate of injection. This maintains a very low steady-state value of $[H_2O_2]$ throughout etching. Thus, if we were to extrapolate the ρ dependence of etching in the presence of Ag to other metals, the current-doubling pathway should be the dominant one for LL-

https://dx.doi.org/10.1021/acsami.0c13980
ACS Appl. Mater. Interfaces 2020, 12, 48969−48981

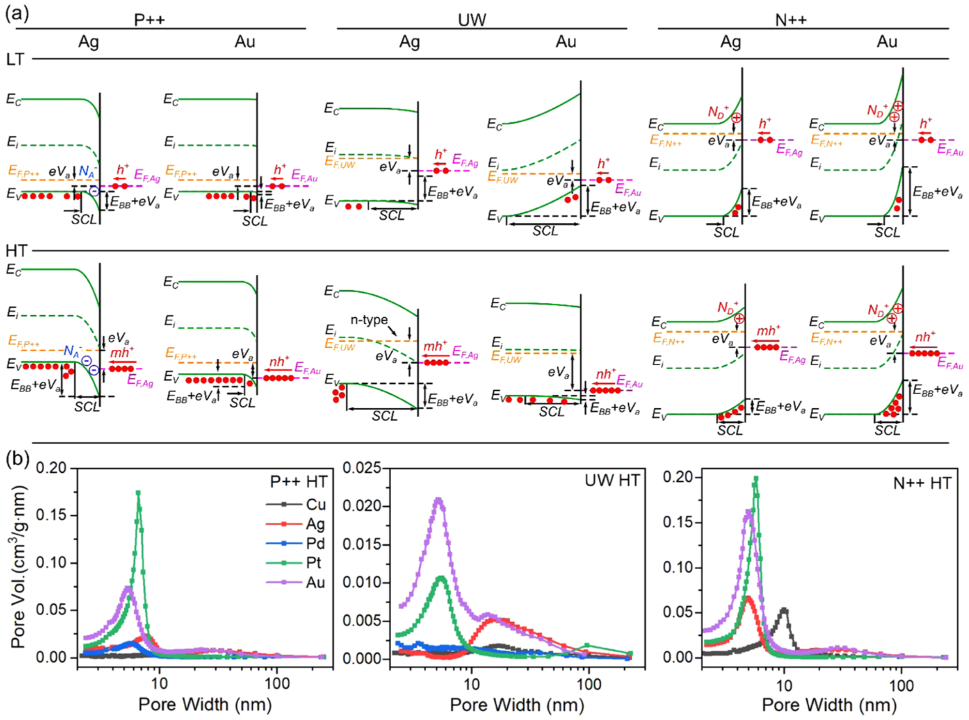

Figure 7. (a) Schematic energy band diagrams for Ag and Au LL-MACE of P++, UW, and N++ powders at low (LT, ice bath) and high (HT, water bath at 43 °C) temperatures. Number of injected holes at HT is larger than at LT and is different for Ag and Au. Due to hole accumulation in the metal, the quasi-Fermi level shifts downwards changing the band bending. The holes (h+) are depicted as filled red dots, and the ionized donors ND+ or acceptors NA- in SCLs of N++ and P++ Si are depicted as open circles with a positive or negative sign, respectively. (b) BJH pore size distributions for all metals after LL-MACE of P++, UW, and N++ powders at HT.

MACE regardless of the type of metal because we always perform LL-MACE with a value of ρ very close to 1.

As one can see, eq 2 does not include any information specific to the metal catalyst, which our results demonstrate to play an essential role in MACE. When VO_2^+ is used as an oxidant, the chemical identity of the metal and its catalytic activity change the mechanism of etching from the current-doubling pathway for Ag and Au to a current-quadrupling pathway for Pt and a combination of them for Pd.[32] Unfortunately, the results for H_2O_2 were less distinct, and in ref 32, it was concluded that the effective valence can be affected by many factors including side reactions, temperature, and metal coverage.

Table 2 summarizes the Fermi levels of Si powders used here as well as metal work functions, magnitudes, widths, and classification of band bending in the ideal scenario and equilibrium conditions after metal deposition (no H_2O_2 injection). Details of the calculation of these parameters can be found in Section S15, Supporting Information. The diameter of the metal particles was set to 20 nm. A clear difference can be observed for the p-type Si between Cu, Ag and Pd, Pt, Au. Due to their low work function, Cu and Ag create a hole depletion space-charge layer (SCL) in the p-type Si, while Pd, Pt, and Au with sufficiently high work function such that $\Phi_M > \Phi_{Si}$ result in hole accumulation and partly degenerate SCLs. Au on P++ powder is a particularly interesting case as there is almost no band bending. This represents an Ohmic contact; it follows a linear current−voltage curve and poses no barrier for charge flow. For the n-type Si, all of the metals build up electron depletion SCLs, and metals with high work function may result in inversion layer formation. Note, however, that in real metal/Si contacts the magnitude of band bending is significantly lower than in the ideal case used for calculation here.[38] Therefore, it is unlikely that in real samples inversion and degenerate parts of SCLs are formed.

Overall, the magnitude of band bending depends on the difference between the metal and Si work functions; the latter in turn depends on the Si doping type and density. Additionally, surface states can appear in the Si/metal interface, and the density of these states may largely affect the Si Fermi level up to the point where it gets pinned.[54] This, however, should not be the case, as relatively defect-free hydrogen-terminated surfaces form during MACE in HF-based solutions. Finally, H_2O_2 reduction injects holes and adsorbates can inject either electrons or holes into metal particles; holes then accumulate in particles due to an imbalance between hole generation, consumption, and/or diffusion and make the particles charged. Charge accumulation acts as an applied voltage bias and creates a local electric field, which penetrates into Si as it cannot be efficiently screened by the low concentration of charge carriers. A potential drop at the Si/metal interface due to the bias can also be viewed as a decrease of the quasi-Fermi level[55] in the metal, thus favoring the holes to flow from metal to Si. The applied bias can sufficiently affect band bending and even change the SCL from, e.g., depletion to accumulation or the reverse.

Chiappini et al.[31] showed the difference in porosity for Si NWs after Ag and Au HL-MACE of the p-type Si at various H_2O_2 concentrations. It is widely accepted that porosity is introduced by remote etching, i.e., the nonlocal etching induced by holes further away from their injection site at the metal/Si interface. The tortuous pores in LL-MACE are due to remote etching, and we demonstrate here that remote etching depends heavily on band bending.

Herein, we discuss a model that considers the rate of hole generation at the solution/metal interface and the rate of hole escape from the metal/Si interface. The balance of these rates determines the balance between local and remote etching. We assume that the rate of escape does not influence the rate of generation. As we shall see, to a first approximation, this model explains the trends found in our data. A further refinement would include the potential for the coupling of these two rates.

In LL-MACE, we used the same amount of H_2O_2 in all etchings. Thus, we assume that the role of H_2O_2 concentration in increasing carrier density is similar to that of temperature, in that either the increase of temperature or increase of H_2O_2 concentration increases the availability of holes.[33,57] Even though the total amount of injected H_2O_2 is independent of temperature, the rate of injection is higher at higher temperatures because of faster diffusion and possible changes in the ratio of H_2O_2 used in hole injection versus side reactions. We further assume that each metal particle accumulates the same number of holes at each temperature independent of the Si doping type. For example, Ag accumulates holes at a certain rate at LT for all Si types and at a higher rate at HT, but again the rate is the same for all Si types. Also, Au accumulates holes at a different rate than Ag at LT and at HT, but still, the rate is the same for all Si types.

During H_2O_2 reduction, metal particles accumulate a positive charge, which acts as the applied potential and lowers the quasi-Fermi level of the metal. This in turn leads to a decrease of band bending in the presence of H_2O_2, $E_{BB}^{H_2O_2}$, by the value of eV_a from the ideal equilibrium values, E_{BB}, listed in Table 2

$$E_{BB}^{H_2O_2} = E_{BB} + eV_a \tag{4}$$

where a potential V_a is gained due to accumulation of N_h holes and can be estimated as[50]

$$V_a = \frac{1}{4\pi\varepsilon_0}\frac{eN_h}{r_M} \tag{5}$$

where ε_0 is the dielectric permittivity of vacuum, e is the elementary charge (positive), and r_M is the radius of the metal particle. With temperature increase, more holes accumulate in the metal lowering its quasi-Fermi level, increasing applied potential V_a, and decreasing band bending.

We first focus on explaining the differences between Ag and Au because these are the two most often used metals in HL-MACE, and in LL-MACE, they exhibit clearly distinctive pore size distributions. For P++ Si, Ag and Au at equilibrium create hole depletion and weak accumulation SCLs, respectively (Table 2). Accumulation of holes in the metal always results in the decrease of its quasi-Fermi level, thus either making depletion stronger, as for Ag, or creating a weak depletion SCL, as in the case of Au (Figure 7a). The striking difference between <10 nm pore volumes can be observed in Figures 7b and S9.1−S9.3, Supporting Information. In contrast, the volumes of etch track pores >10 nm produced by the metal particle movement are nearly identical. Thus, the availability of holes used for the above-critical-current etching near the particles is similar for Ag and Au, whereas the availability of holes that induce remote etching is minimal for Ag.

The Ag deposition-induced depletion SCL in P++ Si efficiently pushes the injected holes and holes present due to doping ($N_A = 4 \times 10^{18}$ cm^{-3}) away from the metal/Si interface. Part of the injected holes may additionally recombine with the fixed negatively charged acceptors N_A^- in the SCL. The layer is, however, rather thin (∼10 nm, Table 2) due to high doping density. Thus, assuming the distance between 20 nm metal particles is on the order of their size or larger,[20] there are regions of Si surface that are not affected by hole depletion. Combined with a high abundance of holes in the bulk and electric fields created by charged metal particles, holes can end up near the Si surface away from the SCL and, although not very efficient, nonetheless induce remote etching of tortuous pores. At HT, more holes get injected into the metal than at LT, decreasing the quasi-Fermi energy. This leads to the increase of potential eV_a, making depletion even stronger while slightly increasing the width of SCL. On the other hand, correspondingly more holes are injected into Si resulting in a higher volume of tortuous pores at HT than at LT (graphs for Ag in Figure 4).

Band bending in P++ Si after Au deposition differs from that induced by Ag (Figure 6a). Since $\Phi_{Au} \sim \Phi_{Si,P++}$, a nearly Ohmic contact is formed with almost flat bands (weak accumulation SCL; Table 2). Thus, there should be no regions of Si where holes are unable to reach the Si surface and participate in remote etching. However, during H_2O_2 injection, a potential eV_a builds up that affects depletion layer formation, and at LT, the volume of pores <10 nm is small (Figures 4 and S9.1, Supporting Information). With the increase of temperature, more holes get injected, and due to much weaker and shorter depletion than in the case of Ag, a lot of tortuous pores are etched (Figures 4 and 7).

Properties of SCLs in UW differ considerably from P++ Si. In addition to metal work functions, Si doping density affects two main parameters of the band bending. First, $E_{F,UW}$ is now close to the middle of the band gap, changing the value of $\Phi_M - \Phi_{Si,UW}$ and, therefore, the magnitude of band bending. Second, low dopant density makes the SCL span over several micrometers (Table 2) covering the whole Si surface. Thus, there is no gap between metal particles where an SCL does not exist. Due to $\Phi_{Ag} \sim \Phi_{Si,UW}$, a weak depletion layer is formed at equilibrium, which becomes stronger during the injection of H_2O_2 as the Ag quasi-Fermi level decreases. However, there are almost no free holes present in bulk UW Si compared to those in P++ Si, and all of the holes injected to Si either diffuse deep into the bulk or participate in local etching in the vicinity of Ag particles, producing only etch track pores (Figures 3 and S11.1, Supporting Information). High temperature makes depletion even stronger by an increase of eV_a. Thus, all holes, which did not participate in local etching, travel away from the Si surface, and no tortuous pores are etched (Figures 4 and 7).

The large work function of Au means that $\Phi_{Au} > \Phi_{Si,UW} > \Phi_{Ag}$, and at equilibrium, Au creates a hole accumulation SCL in UW Si (Figure 7a). It is again spatially large as there are almost no holes from dopants to compensate the negative charge in Au. During H_2O_2 injection at LT, the magnitude of SCL somewhat decreases, which, however, is not enough to fully compensate the band bending. Thus, most of the holes accumulate at the Au/Si interface and are consumed for local etching of etch track pores (Figures 4 and S11.1, Supporting Information). The situation, however, changes significantly at HT when more holes are injected into Au, further lowering the magnitude of band bending. We assume that eV_a at HT becomes large enough to almost completely eliminate band bending, creating an Ohmic contact or a slight hole depletion layer. This would efficiently inject holes from Au into Si and spread them across the whole Si particle with virtually no barrier to approach the surface to participate in remote etching. We indeed clearly observed a significant increase of tortuous pore volume and specific surface area with the increase of temperature for UW Au LL-MACE (Figures 4 and S11.1−S11.3, Supporting Information).

Considering N++ powder, we note that there are extremely few holes present at equilibrium in Si, and its $E_{F,N++}$ is quite close to the conduction band, making $\Phi_{Si,N++} < \Phi_{Me}$ for all metals. Thus, both Ag and Au create electron depletion layers consisting of fixed ionized donors N_D^+, which are positively charged phosphorus atoms as their electrons diffused into the metal due to differences in work functions (Figure 7a). When band bending is strong enough, the intrinsic level E_i can cross $E_{F,N++}$. Then, according to the definition of the p-type Si, N++ Si changes from n-type to p-type in the area of SCL, where $E_i > E_{F,N++}$. An inversion layer is formed for all of the metals except Ag in the equilibrium conditions and ideal band bending. We, however, point out again that the formation of an inversion layer on real Si surfaces without the additional applied bias is highly unlikely.[38] In most cases, only an electron depletion layer is built up with a width of 8−10 nm instead of ~27 nm as listed in Table 2 for ideal band bending case (but see the discussion of Pd and Pt after Ag and Au).

Similar to UW Si and if no inversion layer is formed, only the holes available during LL-MACE of N++ Si with Ag and Au are the holes injected first into the metal particles by H_2O_2 reduction, which subsequently diffused into Si. Herein, we note the approximately twice higher volume of tortuous pores etched by both Ag and Au in N++ Si compared to that of P++ Si (Figures 4 and 6). We propose that in addition to SCL differences, two other factors play significant roles here. The first one is the charged donors in the N++ electron depletion SCL, which may take part in LL-MACE and at least partially take a role of holes to induce etching. Since donors are fixed in the Si lattice, they are not susceptible to diffusion, and it can be shown that all donors are ionized in the SCL.[54] The second and more important factor is the many orders of magnitude larger hole diffusion current in N++ compared to that in P++. To produce the observed yields, the number of holes injected by H_2O_2 dissociation and consumed per Si particle during etching is on the order of 4×10^{10} s^{-1}. This value is slightly higher than $N_h = 2.3 \times 10^{10}$ per Si particle in P++ powder and 10^{17} times larger than $N_h = 1.5{\cdot}10^{-7}$ per Si particle in N++ powder. Thus, in N++ Si due to the large difference between the density of injected holes compared to the equilibrium density of holes, the SCL cannot act as a reservoir to counteract the redistribution of these holes from their site of injection. This leads to efficient hole diffusion away from metal particles and etching of numerous tortuous pores despite the recombination of injected holes with bulk electrons.

Pd and Pt are the two metals with the largest work functions among the set of metals studied. Both create upward band bending independent of Si type, producing hole accumulation layers in the p-type Si and electron depletion layers in the n-type Si (Table 2). $\Phi_{Pt} > \Phi_{Pd}$ and consequently ideal magnitudes of band bending are the highest for Pt. Thus, we cannot exclude the formation of an inversion layer with mobile holes in N++ Si. Indeed, we observed slow gas bubble generation for both Pt- and Pd-deposited N++ Si even without H_2O_2 injection, which indicated the presence of slow etching. No gas generation was found for other Si grades and metals after deposition.

Pt was highly efficient in the etching of tortuous pores in all Si grades with the highest values of v_{pore}/v_{etched} (Figures 4, 5, and S12.2, Supporting Information). We attribute this to several factors. First, Pt particles tended to aggregate to a smaller number of larger chunks (Figures 2 and 3); etching of etch track pores by the aggregates was rather local, possibly due to the prevalence of the current-quadrupling pathway for Pt MACE.[32] Second, the high magnitude of band bending resulted in hole accumulation SCL for the p-type Si and buildup of an inversion layer in the n-type Si. Finally, the SCLs are wide enough to span between metal particles attracting holes to the Si surface and inducing remote etching. The only metal that was able to outperform Pt to create higher volumes of tortuous pores and specific surface area was Au and only for UW at HT: 0.038 versus 0.106 $cm^3{\cdot}g^{-1}$ (Figures 4, 5, and 7b and Tables S6.4 and S7.4, Supporting Information). We propose that the Pt-induced band bending favors the injected hole accumulation near the Si surface and makes more holes available for participation in etching than for Au. With temperature increase, this leads to increased local etching, which can be clearly observed by the growth of the average pore size and decrease of v_{pore}/v_{etched} ratio. On the other hand, due to the large distance between aggregated Pt particles, there is more Si without SCL where hole diffusion current brings holes to produce tortuous pores.

The behavior of Pd is the most unique. Based on the discussion above, it should produce porosity somewhere between Au and Pt. However, this is not the case. Moreover, 25 μmol of Pd as used for other metals resulted in complete dissolution of Si. Consequently, we used 2.5 μmol for all of the etchings with Pd presented here, yet still, the outcome of LL-MACE was very different. Electropolishing was observed for UW powder at all temperatures, while for P++ wafer the volume of tortuous pores decreased with increasing temperature (Figure 3 and Table S5.2, Supporting Information). For N++ powder, etching was noticed after Pd deposition similar to Pt. Thus, Φ_{Pd} may be high enough to create an inversion SCL in Si. Additionally, Pd itself was found to be highly catalytically active toward etching of Si even without oxidant injection, which was attributed to the effects of dissolved O_2.[58] Consistent with the concurrent etching by both valence 2 and valence 4 paths of etching reported by Kolasinski et al.,[32] Pd seems to catalyze electropolishing instead of tortuous pore formation, especially at HT.

Among all of the tested metals, Cu dissolves most readily upon H_2O_2 injection because it has the lowest reduction potential. For example, Cao et al.[59] measured nearly 90% Cu mass reduction during the first 60 s of MACE. Therefore, no HL-MACE was reported with Cu to produce ordered arrays of etch track pores and Si NWs, although surface roughening was a common outcome.[60,61] Furthermore, the band bending induced by Cu is similar to Ag; it is unfavorable for remote etching as a depletion SCL is formed in the p-type Si (Table 2). For UW, only etch track pores were observed analogous to Ag (Figure 4). With temperature increase, the reduction of H_2O_2 becomes faster and more Cu is dissolved than at LT. We associate the Cu dissolution with a significant change of pore size distributions with temperature for P++ and N++ powders and electropolishing for UW powder (Figures 4 and 7b) compared to other metals. Therefore, only at LT, a reasonable volume of tortuous pores was etched for P++ Si and etch track pores for UW Si. On the other hand, the yield was 72 and 78% for P++ and UW, respectively, clearly indicating only partial etching of Si particles (Figures 2 and 5). When most of the Cu is dissolved, etching may switch to a more regenerative electroless etching-like mechanism.[27] In this case, Cu ions inject holes into Si directly and then get regenerated by H_2O_2 to repeat the process. At HT, the rate of injection increases, resulting in electropolishing, while some etch track pores produced by large Cu particles are still generated.

Intermediately doped P+, P, and N+ Si powders show nearly the same outcomes as UW Si for each metal (Figure 6). These results support the previous assumption that the injection of holes into Si is independent of Si grade and is determined mainly by the metal. Since the rate of holes that must be injected per Si particle is on the order of 4×10^{10} s^{-1}, which is much larger than the number of dopant atoms in the particle, there is a large gradient in hole concentration between the metal nanoparticle and bulk Si. The large gradient then drives the diffusion of holes from the metal into the Si bulk, and some of the holes re-emerge near the Si surface to induce remote etching. The appearance of holes far from metal nanoparticles near the Si surface is in turn governed by the type of SCL, magnitude of the electric field in it, and SCL width. For P+, P, UW, and N+ powders, SCL width becomes large enough to leave no gaps between metal nanoparticles (Table 2). Thus, depending on the type of SCL, holes get effectively pushed into the bulk by the electric field (as for Cu and Ag) or stay close to metal nanoparticles (as for Pd, Pt, and Au). Only when there are enough holes accumulated in Au at HT and the magnitude of band bending on the Si/Au interface along with the electric field is decreased, holes are able to diffuse further from metal nanoparticles and tortuous pores start to appear. Pt is the exception here; it produces tortuous pores for all Si grades and at all temperatures (Figures 4 and 6 and Section S6, Supporting Information). In our view, this is due to upward band bending in all Si grades and large size of Pt nanoparticle aggregates. The latter results in the parts of Si surface not affected by SCL.

The rate of hole generation in metal nanoparticles, their charging, and further diffusion of holes into Si are affected by H_2O_2 concentration near the nanoparticles. During etching, the H_2O_2 needs to diffuse from the injection site in the solution, thus making the H_2O_2 concentration in the pores unknown. The size of metal nanoparticles and correspondingly the size of etch track pores may therefore play an important role in the transport of H_2O_2 and other species involved in etching. For example, a few large metal nanoparticles (as in the case of Pt) generate wider etch track pores that facilitate a faster influx of etchant and efflux of etch products. A steady-state concentration gradient may be reached around metal particles in the tortuous pores due to the balance between the reaction and diffusion rates. Concentration gradient profiles can be further affected by, e.g., temperature, metal catalyst, pore size, and depth and contribute to the pore morphology of the product.

To summarize, LL-MACE resulted in distinctive specific surface areas, yields, and pore volumes depending on the Si grade, metal catalyst, and temperature. Three major factors have been identified that contribute to the distinctive features of LL-MACE:

(1) Band bending and space-charge layer (SCL) formation clearly play a significant role in defining the observed outcomes. A distinct difference exists between the highly doped nearly metallic Si and moderately doped Si. The SCL width in relation to the distance between metal nanoparticles is crucial. The SCL is narrow for N++ and P++ Si, leaving gaps on the Si surface between metal nanoparticles without the electric field. For HL-MACE, it is believed that remote etching is only important in P++ Si. In LL-MACE, we find that the orders of magnitudes larger gradient of hole concentration in N++ facilitate high hole diffusion current and efficient remote etching.

(2) Chemical, not just electronic, differences between metals lead to distinctive behaviors. Dissolution and redeposition of metal nanoparticles affect the nanoparticle structure during etching, which in turn affects the resulting pore size distributions. We observed peculiar comet-like structures of Cu, Pd, and Pt particles (Figure 2), which unambiguously demonstrates the dynamic nature of metal nanoparticles. The comet-like structure is not required for remote etching because Au never shows a comet-like structure and Pt does not always show it even though they are efficient catalysts of remote etching. The reactivity of Pd is unique, and it must be used at a lower coverage than the other metals to enable porosification.

(3) Mass transport and concentration of H_2O_2 affect the rates of both etching and metal nanoparticle dissolution and are important for morphological evolution. Cu is the most easily dissolving metal, and at high temperature, it catalyzes electropolishing rather than porosification. Nonetheless, a low concentration of H_2O_2 achieved with controlled injection and low temperature enables highly efficient and controllable LL-MACE also with Cu (Figures 3 and 4).

■ CONCLUSIONS

Our comprehensive study has illuminated the mechanisms of MACE and enhanced our ability to exploit it for technical applications. We built upon the recognition of the role of band bending in Si[39] in the vicinity of deposited metal nanoparticles[38,62] to gain control over the structures formed by etching. We show that band bending alone is unable to fully describe the observed LL-MACE outcomes. Instead, the chemical identity of metals, their catalytic activity toward the reduction of H_2O_2, the ability to induce different etching pathways, and the tendency to dissolve all influence the results of etching. We demonstrated the generality of LL-MACE and that it can be applied to any kind of Si. Moreover, the judicious choice of the etching parameters (including H_2O_2 concentration, metal catalyst, temperature, and the type and density of Si doping) facilitates considerable control of the mean pore size, surface areas, and pore volumes of etched Si powders. The large variety of accessible surface areas, pore sizes, and pore volumes combined with high scalability and economical use of reagents will make LL-MACE highly appealing for use in both research and industry.

■ ASSOCIATED CONTENT

Supporting Information

The Supporting Information is available free of charge at https://pubs.acs.org/doi/10.1021/acsami.0c13980.

Experimental details, description of band bending calculation, and detailed etching data for all Si types including metallurgical-grade Si (PDF)

■ AUTHOR INFORMATION

Corresponding Author

Kurt W. Kolasinski − *Department of Chemistry, West Chester University, West Chester, Pennsylvania 19383-2115, United States;* orcid.org/0000-0002-9469-2700; Email: KKolasinski@wcupa.edu

Authors

Konstantin Tamarov − *Department of Applied Physics, University of Eastern Finland, 70210 Kuopio, Finland;* orcid.org/0000-0003-0087-4878

Riku Kiviluoto − *Department of Applied Physics, University of Eastern Finland, 70210 Kuopio, Finland*

Joseph D. Swanson − *Department of Chemistry, West Chester University, West Chester, Pennsylvania 19383-2115, United States*

Bret A. Unger − *Department of Chemistry, West Chester University, West Chester, Pennsylvania 19383-2115, United States*

Alexis T. Ernst − *Department of Materials Science and Engineering, Institute of Materials Science, University of Connecticut, Storrs, Connecticut 06269-3136, United States*

Mark Aindow − *Department of Materials Science and Engineering, Institute of Materials Science, University of Connecticut, Storrs, Connecticut 06269-3136, United States;* orcid.org/0000-0001-6617-1409

Joakim Riikonen − *Department of Applied Physics, University of Eastern Finland, 70210 Kuopio, Finland;* orcid.org/0000-0002-5304-9479

Vesa-Pekka Lehto − *Department of Applied Physics, University of Eastern Finland, 70210 Kuopio, Finland;* orcid.org/0000-0001-8153-1070

Complete contact information is available at: https://pubs.acs.org/10.1021/acsami.0c13980

Author Contributions

The manuscript was written through the contributions of all authors. All authors have given approval to the final version of the manuscript.

Funding

Funding provided by grants #314552 and #314412 from the Academy of Finland and the National Science Foundation award #1825331.

Notes

The authors declare no competing financial interest.

■ ACKNOWLEDGMENTS

The microscopy studies were performed using the facilities in the UConn/Thermo Fisher Scientific Center for Advanced Microscopy and Materials Analysis (CAMMA) and SIB Labs, Laboratory of Microscopy, at the University of Eastern Finland. Silicon was provided by Elkem Silicon Materials and Okmetic.

■ REFERENCES

(1) Peng, K. Q.; Lee, S. T. Silicon Nanowires for Photovoltaic Solar Energy Conversion. *Adv. Mater.* **2011**, *23*, 198−215.

(2) Otto, M.; Algasinger, M.; Branz, H.; Gesemann, B.; Gimpel, T.; Füchsel, K.; Käsebier, T.; Kontermann, S.; Koynov, S.; Li, X.; Naumann, V.; Oh, J.; Sprafke, A. N.; Ziegler, J.; Zilk, M.; Wehrspohn, R. B. Black Silicon Photovoltaics. *Adv. Opt. Mater.* **2015**, *3*, 147−164.

(3) Toor, F.; Miller, J. B.; Davidson, L. M.; Duan, W.; Jura, M. P.; Yim, J.; Forziati, J.; Black, M. R. Metal Assisted Catalyzed Etched (MACE) Black Si: Optics and Device Physics. *Nanoscale* **2016**, *8*, 15448−15466.

(4) Sainato, M.; Strambini, L. M.; Rella, S.; Mazzotta, E.; Barillaro, G. Sub-Parts per Million NO2 Chemi-Transistor Sensors Based on Composite Porous Silicon/Gold Nanostructures Prepared by Metal-Assisted Etching. *ACS Appl. Mater. Interfaces* **2015**, *7*, 7136−7145.

(5) Balderas-Valadez, R. F.; Agarwal, V.; Pacholski, C. Fabrication of Porous Silicon-Based Optical Sensors Using Metal-Assisted Chemical Etching. *RSC Adv.* **2016**, *6*, 21430−21434.

(6) Georgobiani, V. A.; Gonchar, K. A.; Zvereva, E. A.; Osminkina, L. A. Porous Silicon Nanowire Arrays for Reversible Optical Gas Sensing. *Phys. Status Solidi A* **2018**, *215*, No. 1700565.

(7) Zamfir, M. R.; Nguyen, H. T.; Moyen, E.; Lee, Y. H.; Pribat, D. Silicon Nanowires for Li-Based Battery Anodes: A Review. *J. Mater. Chem. A* **2013**, *1*, 9566−9586.

(8) Li, X.; Yan, C.; Wang, J.; Graff, A.; Schweizer, S. L.; Sprafke, A.; Schmidt, O. G.; Wehrspohn, R. B. Stable Silicon Anodes for Lithium-Ion Batteries Using Mesoporous Metallurgical Silicon. *Adv. Energy Mater.* **2015**, *5*, No. 1401556.

(9) McSweeney, W.; Geaney, H.; O'Dwyer, C. Metal-Assisted Chemical Etching of Silicon and the Behavior of Nanoscale Silicon Materials as Li-Ion Battery Anodes. *Nano Res.* **2015**, *8*, 1395−1442.

(10) Han, H.; Kim, J.; Shin, H. S.; Song, J. Y.; Lee, W. Air-Bridged Ohmic Contact on Vertically Aligned Si Nanowire Arrays: Application to Molecule Sensors. *Adv. Mater.* **2012**, *24*, 2284−2288.

(11) Chiappini, C.; De Rosa, E.; Martinez, J. O.; Liu, X.; Steele, J.; Stevens, M. M.; Tasciotti, E. Biodegradable Silicon Nanoneedles Delivering Nucleic Acids Intracellularly Induce Localized in Vivo Neovascularization. *Nat. Mater.* **2015**, *14*, 532−539.

(12) Harding, F. J.; Surdo, S.; Delalat, B.; Cozzi, C.; Elnathan, R.; Gronthos, S.; Voelcker, N. H.; Barillaro, G. Ordered Silicon Pillar Arrays Prepared by Electrochemical Micromachining: Substrates for High-Efficiency Cell Transfection. *ACS Appl. Mater. Interfaces* **2016**, *8*, 29197−29202.

(13) Osminkina, L. A.; Sivakov, V. A.; Mysov, G. A.; Georgobiani, V. A.; Natashina, U. A.; Talkenberg, F.; Solovyev, V. V.; Kudryavtsev, A. A.; Timoshenko, V. Y. Nanoparticles Prepared from Porous Silicon Nanowires for Bio-Imaging and Sonodynamic Therapy. *Nanoscale Res. Lett.* **2014**, *9*, 463.

(14) Peng, F.; Su, Y.; Wei, X.; Lu, Y.; Zhou, Y.; Zhong, Y.; Lee, S.-T.; He, Y. Silicon-Nanowire-Based Nanocarriers with Ultrahigh Drug-Loading Capacity for In Vitro and In Vivo Cancer Therapy. *Angew. Chem., Int. Ed.* **2013**, *52*, 1457−1461.

(15) Peng, F.; Su, Y.; Ji, X.; Zhong, Y.; Wei, X.; He, Y. Doxorubicin-Loaded Silicon Nanowires for the Treatment of Drug-Resistant Cancer Cells. *Biomaterials* **2014**, *35*, 5188−5195.

(16) Huang, Z.; Geyer, N.; Werner, P.; de Boor, J.; Gösele, U. Metal-Assisted Chemical Etching of Silicon: A Review. *Adv. Mater.* **2011**, *23*, 285−308.

(17) Chen, C.-Y.; Wei, T.-C.; Hsiao, P.-H.; Hung, C.-H. Vanadium Oxide as Transparent Carrier-Selective Layer in Silicon Hybrid Solar Cells Promoting Photovoltaic Performances. *ACS Appl. Energy Mater.* **2019**, *2*, 4873−4881.

(18) Putra, I. R.; Li, J.-Y.; Chen, C.-Y. 18.78% Hierarchical Black Silicon Solar Cells Achieved with the Balance of Light-Trapping and Interfacial Contact. *Appl. Surf. Sci.* **2019**, *478*, 725−732.

(19) Kolasinski, K. W.; Unger, B. A.; Ernst, A. T.; Aindow, M. Crystallographically Determined Etching and Its Relevance to the Metal-Assisted Catalytic Etching (MACE) of Silicon Powders. *Front. Chem.* **2019**, *6*, No. 651.

(20) Tamarov, K. P.; Swanson, J. D.; Unger, B. A.; Kolasinski, K. W.; Ernst, A. T.; Aindow, M.; Lehto, V.-P.; Riikonen, J. Controlling the Nature of Etched Si Nanostructures: High versus Low Load Metal-Assisted Catalytic Etching (MACE) of Si Powders. *ACS Appl. Mater. Interfaces* **2020**, *12*, 4787−4796.

(21) Li, X.; Xiao, Y.; Yan, C.; Zhou, K.; Miclea, P. T.; Meyer, S.; Schweizer, S. L.; Sprafke, A.; Lee, J. H.; Wehrspohn, R. B. Self-Purification Model for Metal-Assisted Chemical Etching of Metallurgical Silicon. *Electrochim. Acta* **2014**, *138*, 476−480.

(22) Xi, F.; Li, S.; Ma, W.; Ding, Z.; Lei, Y.; Chen, Z.; Wei, K.; Xie, K.; Wu, J. Removal of Impurities from Metallurgical Grade Silicon with Metal Assisted Chemical Leaching. *Hydrometallurgy* **2018**, *178*, 250−255.

(23) Liu, Y.; Chen, B.; Cao, F.; Chan, H. L. W.; Zhao, X.; Yuan, J. One-Pot Synthesis of Three-Dimensional Silver-Embedded Porous Silicon Micronparticles for Lithium-Ion Batteries. *J. Mater. Chem.* **2011**, *21*, 17083−17086.

(24) Bang, B. M.; Kim, H.; Song, H.-K.; Cho, J.; Park, S. Scalable Approach to Multi-Dimensional Bulk Si Anodes via Metal-Assisted Chemical Etching. *Energy Environ. Sci.* **2011**, *4*, 5013−5019.

(25) Li, X.; Xiao, Y.; Bang, J. H.; Lausch, D.; Meyer, S.; Miclea, P.; Jung, J.; Schweizer, S. L.; Lee, J.; Wehrspohn, R. B. Upgraded Silicon Nanowires by Metal-Assisted Etching of Metallurgical Silicon: A New Route to Nanostructured Solar-Grade Silicon. *Adv. Mater.* **2013**, *25*, 3187−3191.

(26) Kozlov, N. K.; Natashina, U. A.; Tamarov, K. P.; Gongalsky, M. B.; Solovyev, V. V.; Kudryavtsev, A. A.; Sivakov, V.; Osminkina, L. A. Recycling of Silicon: From Industrial Waste to Biocompatible Nanoparticles for Nanomedicine. *Mater. Res. Express* **2017**, *4*, No. 095026.

(27) Kolasinski, K. W.; Gimbar, N. J.; Yu, H.; Aindow, M.; Mäkilä, E.; Salonen, J. Regenerative Electroless Etching of Silicon. *Angew. Chem., Int. Ed.* **2017**, *56*, 624−627.

(28) Alhmoud, H.; Brodoceanu, D.; Elnathan, R.; Kraus, T.; Voelcker, H. A MACEing Silicon: Towards Single-Step Etching of Defined Porous Nanostructures for Biomedicine. *Prog. Mater. Sci.* **2019**, No. 100636.

(29) Geyer, N.; Wollschläger, N.; Fuhrmann, B.; Tonkikh, A.; Berger, A.; Werner, P.; Jungmann, M.; Krause-Rehberg, R.; Leipner, H. S. Influence of the Doping Level on the Porosity of Silicon Nanowires Prepared by Metal-Assisted Chemical Etching. *Nanotechnology* **2015**, *26*, No. 245301.

(30) Georgobiani, V. A.; Gonchar, K. A.; Osminkina, L. A.; Timoshenko, V. Y. Structural and Photoluminescent Properties of Nanowires Formed by the Metal-Assisted Chemical Etching of Monocrystalline Silicon with Different Doping Level. *Semiconductors* **2015**, *49*, 1025−1029.

(31) Chiappini, C.; Liu, X.; Fakhoury, J. R.; Ferrari, M. Biodegradable Porous Silicon Barcode Nanowires with Defined Geometry. *Adv. Funct. Mater.* **2010**, *20*, 2231−2239.

(32) Kolasinski, K. W.; Barclay, W. B.; Sun, Y.; Aindow, M. The Stoichiometry of Metal Assisted Etching (MAE) of Si in V_2O_5 + HF and HOOH + HF Solutions. *Electrochim. Acta* **2015**, *158*, 219−228.

(33) Kolasinski, K. W. Electron Transfer during Metal-Assisted and Stain Etching of Silicon. *Semicond. Sci. Technol.* **2016**, *31*, No. 014002.

(34) Yae, S.; Tashiro, M.; Hirano, T.; Abe, M.; Fukumuro, N.; Matsuda, H. High Catalytic Activity of Palladium for Metal-Enhanced Hydrofluoric Acid Etching of Silicon. *ECS Trans.* **2009**, *16*, 285−289.

(35) Lee, J. P.; Choi, S.; Park, S. Extremely Superhydrophobic Surfaces with Micro- and Nanostructures Fabricated by Copper Catalytic Etching. *Langmuir* **2011**, *27*, 809−814.

(36) Guan, B.; Sun, Y.; Li, X.; Wang, J.; Chen, S.; Schweizer, S.; Wang, Y.; Wehrspohn, R. B. Conversion of Bulk Metallurgical Silicon into Photocatalytic Nanoparticles by Copper-Assisted Chemical Etching. *ACS Sustainable Chem. Eng.* **2016**, *4*, 6590−6599.

(37) Huang, Z. P.; Geyer, N.; Liu, L. F.; Li, M. Y.; Zhong, P. Metal-Assisted Electrochemical Etching of Silicon. *Nanotechnology* **2010**, *21*, No. 465301.

(38) Kolasinski, K. W. The Mechanism of Galvanic/Metal-Assisted Etching of Silicon. *Nanoscale Res. Lett.* **2014**, *9*, No. 432.

(39) Torralba, E.; Le Gall, S.; Lachaume, R.; Magnin, V.; Harari, J.; Halbwax, M.; Vilcot, J.-P.; Cachet-Vivier, C.; Bastide, S. Tunable Surface Structuration of Silicon by Metal Assisted Chemical Etching with Pt Nanoparticles under Electrochemical Bias. *ACS Appl. Mater. Interfaces* **2016**, *8*, 31375−31384.

(40) Kolasinski, K. W. The Mechanism of Si Etching in Fluoride Solutions. *Phys. Chem. Chem. Phys.* **2003**, *5*, 1270−1278.

(41) Hochbaum, A. I.; Gargas, D.; Hwang, Y. J.; Yang, P. Single Crystalline Mesoporous Silicon Nanowires. *Nano Lett.* **2009**, *9*, 3550−3554.

(42) Patil, J. J.; Smith, B. D.; Grossman, J. C. Ultra-High Aspect Ratio Functional Nanoporous Silicon via Nucleated Catalysts. *RSC Adv.* **2017**, *7*, 11537−11542.

(43) Klaassen, D. B. M. A Unified Mobility Model for Device Simulation—I. Model Equations and Contentration Dependence. *Solid. State. Electron.* **1992**, *35*, 961−967.

(44) Kolasinski, K. W.; Barclay, W. B. The Stoichiometry of Electroless Silicon Etching in Solutions of V_2O_5 and HF. *Angew. Chem., Int. Ed.* **2013**, *52*, 6731−6734.

(45) Kolasinski, K. W. Silicon Nanostructures from Electroless Electrochemical Etching. *Curr. Opin. Solid State Mater. Sci.* **2005**, *9*, 73−83.

(46) Gondek, C.; Lippold, M.; Röver, I.; Bohmhammel, K.; Kroke, E. Etching Silicon with HF-H2O2-Based Mixtures: Reactivity Studies and Surface Investigations. *J. Phys. Chem. C* **2014**, *118*, 2044−2051.

(47) Sadakane, D.; Yamakawa, K.; Fukumuro, N.; Yae, S. Catalytic Activity of Ru for Metal-Assisted Etching of Si. *ECS Trans.* **2015**, *69*, 179−184.

(48) Yae, S.; Morii, Y.; Fukumuro, N.; Matsuda, H. Catalytic Activity of Noble Metals for Metal-Assisted Chemical Etching of Silicon. *Nanoscale Res. Lett.* **2012**, *7*, No. 352.

(49) Stafiniak, A.; Prażmowska, J.; Macherzyński, W.; Paszkiewicz, R. Nanostructuring of Si Substrates by a Metal-Assisted Chemical Etching and Dewetting Process. *RSC Adv.* **2018**, *8*, 31224−31230.

(50) Wang, J.; Hu, Y.; Zhao, H.; Fu, H.; Wang, Y.; Huo, C.; Peng, K. Q. Oxidant Concentration Modulated Metal/Silicon Interface Electrical Field Mediates Metal-Assisted Chemical Etching of Silicon. *Adv. Mater. Interfaces* **2018**, *5*, No. 1801132.

(51) Chartier, C.; Bastide, S.; Lévy-Clément, C. Metal-Assisted Chemical Etching of Silicon in HF−H_2O_2. *Electrochim. Acta* **2008**, *53*, 5509−5516.

(52) Xia, X. H.; Ashruf, C. M. A.; French, P. J.; Kelly, J. J. Galvanic Cell Formation in Silicon/Metal Contacts: The Effect on Silicon Surface Morphology. *Chem. Mater.* **2000**, *12*, 1671−1678.

(53) Kooij, E. S.; Vanmaekelbergh, D. Catalysis and Pore Initiation in the Anodic Dissolution of Silicon in HF. *J. Electrochem. Soc.* **1997**, *144*, 1296−1301.

(54) Lüth, H. Space-Charge Layers at Semiconductor Interfaces. In *Solid Surfaces, Interfaces and Thin Films*; Springer, 2015; pp 337−391.

(55) Streetman, B. G.; Banerjee, S. K. *Solid State Electronic Devices*, 6th ed.; Pearson Education, Inc., 2006.

(56) *CRC Handbook of Chemistry and Physics*, 95th ed.; Haynes, W. M., Ed.; CRC Press: Boca Raton, FL, 2014.

(57) Kolasinski, K. W.; Gogola, J. W.; Barclay, W. B. Test of Marcus Theory Predictions for Electroless Etching of Silicon. *J. Phys. Chem. C* **2012**, *116*, 21472−21481.

(58) Yae, S.; Tashiro, M.; Abe, M.; Fukumuro, N.; Matsuda, H. High Catalytic Activity of Palladium for Metal-Enhanced HF Etching of Silicon. *J. Electrochem. Soc.* **2010**, *157*, D90.

(59) Cao, M.; Li, S. Y.; Deng, J. X.; Yang, X. W.; Li, Y. P.; Ma, W. H.; Zhou, Y. Preparation of Large-Area Porous Silicon through Cu-Assisted Chemical Etching. *Mater. Sci. Forum* **2016**, *847*, 78−83.

(60) Toor, F.; Oh, J.; Branz, H. M. Efficient Nanostructured 'Black' Silicon Solar Cell by Copper-Catalyzed Metal-Assisted Etching. *Prog. Photovoltaics* **2015**, *23*, 1375−1380.

(61) Zheng, H.; Han, M.; Zheng, P.; Zheng, L.; Qin, H.; Deng, L. Porous Silicon Templates Prepared by Cu-Assisted Chemical Etching. *Mater. Lett.* **2014**, *118*, 146−149.

(62) Lai, R. A.; Hymel, T. M.; Narasimhan, V. K.; Cui, Y. Schottky Barrier Catalysis Mechanism in Metal-Assisted Chemical Etching of Silicon. *ACS Appl. Mater. Interfaces* **2016**, *8*, 8875−8879.